PAPER

Check for updates

Nano-interfacial interactions in 2-D Ni₃S₂–Ni₃N nanosheets for the hydrogen evolution reaction in an alkaline medium†

Vikas Pundir,‡ Ashish Gaur,‡ Rajdeep Kaur, Aashi and Vivek Bagchi [ID] *

Sustainable hydrogen generation is a necessity for implementing the hydrogen economy of the future. In recent decades, the electrocatalytic hydrogen evolution reaction (HER) has attracted researchers' interest as a key to understanding the mechanism of water electrolysis. Due to the sluggish kinetics of the hydrogen evolution reaction (HER) in alkaline environments, the development of an effective non-noble electrocatalyst for hydrogen generation is crucial but challenging. Herein, the heterostructure of Ni_3S_2–Ni_3N was prepared by a three-step synthesis procedure that consists of the formation of Ni_3S_2 on NF, the electrodeposition of $Ni(OH)_2$ over Ni_3S_2 and nitridation in the presence of ammonia. The interface formation between Ni_3S_2 and Ni_3N was successfully characterized using HRTEM analysis. The HER performance of the catalyst containing a Ni_3S_2–Ni_3N interface was found to be superior to that of individual Ni_3S_2 and Ni_3N phases. An overpotential of 96 mV was obtained for the Ni_3S_2–Ni_3N heterostructured catalyst at a current density of 10 mA cm^{-2} with a Tafel slope value of 135 mV dec^{-1}. The catalyst was stable for 70 h with no loss under high current densities. This study offers a facile and dependable synthetic method for the rational design of extremely potent HER electrocatalysts in alkaline media.
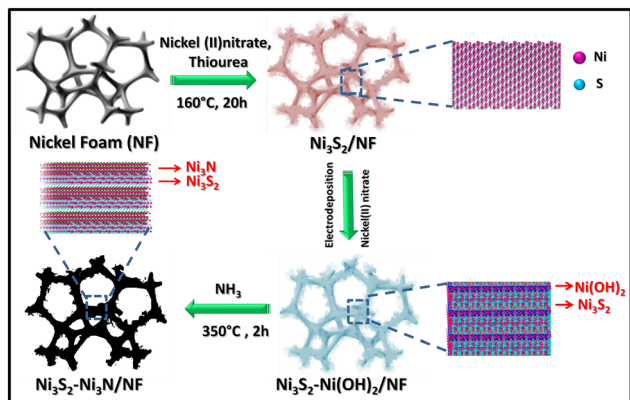
Introduction

Hydrogen, as a sustainable and clean source of energy with a high energy density, has received a lot of attention in recent decades, and it is often regarded as the most viable replacement for conventional fossil fuels. Traditional processes such as catalytic decomposition of natural gas, steam reforming of natural gas, and thermal decomposition of heavy crude are well-established technologies that are already implemented.[1,2] However, owing to huge carbon dioxide emission, exploration of carbon-neutral strategies has been given utmost importance. The generation of green hydrogen in a sustainable path is one of the prime objectives in the recent energy research. In this regard, electrocatalytic water splitting can be a potential technique, which can yield hydrogen using renewable energies.[3–7] The ideal HER catalysts are considered to be the platinum-group (Pt and Ir)-metals and their composites. However, there is a dearth of availability of such metals making them highly expensive and thus limiting their widespread use.[8] As a result, finding effective, inexpensive, and stable catalysts to meet the

ever-increasing hydrogen demand is critical. In order to develop an alternative for the noble metal electrocatalysts, researchers have conducted extensive studies on non-noble metal compounds such as phosphides,[9–12] sulphides,[13–16] oxides[17–20] and nitrides.[21–23] Because of its remarkable catalytic efficiency and minimal cost, transition metal nickel (Ni) has drawn considerable attention for energy conversion reactions.[24,25] Specifically, Ni_3N has received a lot of attention because of its outstanding electrical conductivity. Recent theoretical and experimental results suggest that Ni_3N possesses a high binding affinity for the adsorbates (atomic hydrogen, protons, or water molecules).[26] Theoretical investigations also indicated that Ni_3N is intrinsically metallic and the carrier concentration and the electrical conductivity can be further improved when dimensional confinement is imposed.[27] Moreover, the disordered structure of atomically thin nanosheets could provide more active sites and intimate contact with support electrodes. Hence, substantial work needs to be done in the nano-structuring of Ni_3N materials for achieving a low overpotential, high stability and optimum hydrogen adsorption energy to enhance the HER performance of nickel nitrides under alkaline conditions. In one such report, Gao *et al.* formed $Ni(OH)_2$–Ni_3N nanoarrays on a titanium mesh as a 3-D electrode for alkaline hydrogen evolution reaction. This heterointerface formation greatly enhances the HER performance of $Ni(OH)_2$ and Ni_3N individual electrodes.[28] In another work, Wang *et al.* tremendously enhanced the HER performance of a Ni_3N electrode

Institute of Nano Science and Technology, Sector-81, SAS nagar, Mohali, Punjab 140306, India. E-mail: vivekbagchi@gmail.com, bagchiv@inst.ac.in

‡ Both authors contributed equally.

Scheme 1 The synthesis strategy of the Ni_3S_2–Ni_3N/NF catalyst.

by Co-doping. Doping of Co into Ni_3N nanosheets enhances the redistribution of electrons and optimizes the water absorption energies.[29] Similarly, Ni_3S_2 exhibits superior conductivity and metallic behaviour due to the abundant Ni–Ni bonds. Typically,[30,31] Ni_3S_2 exhibits significant hydrogen (H*) adsorption on Ni–S and Ni–Ni sites but desorption of this intermediate (H*) on these active sites is not promising.[32] Numerous controlled strategies have been developed to address this issue, such as enhancing the inherent conductivity *via* atomic doping,[33] providing extra catalytically active sites by altering the morphology,[34] or lowering the energy barrier by designing a heterostructure with other HER active materials.[35–37] However, heterostructure formation is one of the best ways to create a potential catalyst. In addition to integrating the benefits of individual components, the heterostructured catalysts also exhibit synergistic effects between these individual components to further lower the kinetic energy barriers of the catalytic reaction.[38] Herein, we have fabricated the heterostructures of Ni_3S_2–Ni_3N for the alkaline hydrogen evolution reaction (Scheme 1). The heterostructure of Ni_3S_2–Ni_3N was prepared by a three-step synthesis procedure that consists of the formation of Ni_3S_2 on NF after which the electrodeposition of $Ni(OH)_2$ over Ni_3S_2 is followed by nitridation in the presence of ammonia. We obtained an overpotential of 96 mV for Ni_3S_2–Ni_3N heterostructure nanosheets at a current density of 10 mA cm^{-2} with a Tafel slope value of 136 mV dec^{-1}. The catalyst was stable for 70 h with no significant loss of current density. The enhancement in the catalytic activity of Ni_3S_2–Ni_3N was explained using X-ray photoelectron spectroscopy (XPS) investigations. The charge transfer from Ni_3N to Ni_3S_2 enhances the availability of electrons on the surface of Ni_3S_2. This increase in the charge density on Ni_3S_2 further enhances the overall HER process by availing more electrons for the intermediate adsorption (H$^+$).

Experimental section

Materials

Most of the chemicals were purchased from two reputed chemical companies and were used directly. Nafion perfluorinated resin solution (5 wt% in a mixture of a lower aliphatic alcohol and water, containing 45% water), nickel(II) nitrate hexahydtate ($Ni(NO_3)_2$·$6H_2O$, 99%) and thiourea (CH_4N_2S) were bought from Sigma Aldrich. TCI supplied potassium hydroxide pellets. Deionized water was used for all preparations. Nickel foam (NF) was purchased from Nanoshel.

Synthesis of Ni_3S_2/NF

NF was ultrasonically cleaned in 3M HCl solution, acetone, and DI water for 20 minutes to remove surface grime and oxide coatings. The washed NF was sliced into tiny pieces with a 1 cm × 1.2 cm cross section. After that, the cleaned NF substrate was put into a Teflon-lined autoclave (50 ml) containing 0.5 mmol of nickel nitrate ($Ni(NO_3)_2$·$6H_2O$, 99%) and 0.3 mmol of thiourea (CH_4N_2S) and 20 ml of DI water. The autoclave was then sealed and gradually heated to 160 °C and heating was continued for 20 hours. After the hydrothermal reaction, the light-brown coloured Ni_3S_2 was isolated and washed several times with DI water and ethanol to remove any remaining impurities, then dried overnight in an air oven at 80 °C.

Synthesis of Ni_3S_2–$Ni(OH)_2$

A CHI 760E Electrochemical Workstation was used to conduct the electrodeposition, which featured a three-electrode cell with saturated Ag/AgCl as the reference electrode, a graphitic rod as the counter electrode, and Ni_3S_2@NF used as the working electrode. The electrolyte used in the experiments was 0.1 M $Ni(NO_3)_2$·$6H_2O$ aqueous solution unless otherwise mentioned. All of the electrodeposition tests were done at a constant voltage of −0.7 V *vs.* Ag/AgCl electrode. The $Ni(OH)_2$ film was grown over Ni_3S_2@NF. The catalyst was dried at 60 °C to form Ni_3S_2@$Ni(OH)_2$.

Synthesis of Ni_3S_2–Ni_3N

The as obtained Ni_3S_2–$Ni(OH)_2$ electrode was kept in a tube furnace at 350 °C for 2 h under high purity NH_3 flow. After cooling down the sample, nanostructures of Ni_3S_2–Ni_3N were formed over nickel foam and used for the electrocatalysis. For comparison, pure Ni_3N was prepared by the nitridation of a $Ni(OH)_2$/NF electrode under similar experimental conditions.

Physical characterization

A Bruker Eco D8 ADVANCE X Powder X-ray diffractometer was used to investigate the structural properties of Ni_3S_2–Ni_3N, Ni_3S_2 and Ni_3N. The diffractometer uses a Ni filter that provides Cu K radiation (= 1.54056, 40 kV, and 25 mA) in the 2θ range of 5°–80° with a rise of 0.00190 per step. The morphological examination of Ni_3S_2–Ni_3N was performed using a JEOL JSM-7600F (FESEM) equipped with an energy-dispersive X-ray diffractometer (Bruker). Transmission electron microscopy (TEM, JEOL-2100) performed at 200 kV was used to analyze the fringe-width of the nanocrystallites of Ni_3S_2–Ni_3N, Ni_3S_2 and Ni_3N. X-Ray photoelectron (XPS) spectroscopy was executed on a K-Alpha plus XPS machine of Thermo Fisher Scientific instruments in a vacuum chamber (7×10^{-9} torr) using Al-K$_\alpha$ radiation (1486.6 eV).

Electrochemical measurements

The electrochemical studies were conducted in a standard three electrode-system, with Ag/AgCl serving as the reference

electrode and a graphite rod serving as the counter electrode. The catalyst grown over NF was utilised as the working electrode. The commercially available standard Pt/C was coated over nickel foam by preparing a homogeneous ink by weighing and dissolving 10 mg of Pt/C in 500 μL of DMF with 10 μL of 5% Nafion solution. A homogeneous catalyst slurry was obtained after 120 minutes of sonication and 40 μL of the ink was dropcast over bare nickel foam followed by vacuum drying. Electrochemical studies were done in 1 M KOH and at a 5 mV^{-1} s^{-1} scan rate. All the data were taken using Ag/AgCl as a reference electrode and converted to the E_{RHE} values by the following equation $E_{RHE} = E_{Ag/AgCl} + 0.197 + 0.059 \times pH$. The stability of the catalyst was determined by running chronoamperometry at different current densities. The Tafel slope was estimated by fitting the Tafel equation ($\eta = b \log(j) + a$) to the linear section of the Tafel curve. Electrochemical impedance spectroscopy (EIS) was carried out with an applied potential of 100 mV in the frequency range of 100 000 Hz to 1 Hz.

Results and discussion

The synthetic route of the Ni$_3$S$_2$–Ni$_3$N heterostructure is demonstrated in Scheme 1. To extract the information associated with the nanocrystallites present in the catalyst, powder X-ray diffraction was performed. The PXRD data of Ni$_3$S$_2$–Ni$_3$N are shown in Fig. 1a. The data well matched with the corresponding reported JCPDS data. The diffraction peaks at 21.7°, 31.02°, 37.8°, 39.0°, 49.9°, 50.4°, 55.9°, 69.15 and 77.8° correspond to the (101), (110), (003), (021), (113), (211), (122), (303) and (401) crystal planes of the Ni$_3$S$_2$ phase (PDF no. 44-1418).[39] The other peaks at 38.3°, 42.04°, 44.2°, 58.4°, 70.4° and 78.5° correspond to the (110), (002), (111), (112), (300) and (113) crystal planes of the Ni$_3$N phase.[40] We have also performed the PXRD study of individual Ni$_3$S$_2$ and Ni$_3$N and the information is provided in ESI,† S1 Fig. S1. The investigation of the chemical states of Ni, S and N was done by using X-ray photoelectron

spectroscopy. The XPS spectrum of Ni2p is given in Fig. 1b. The peaks appearing at 852.9, 855.7, and 859.07 eV correspond to Ni^{+1}, Ni^{+2} and one satellite peak of Ni2p$_{3/2}$. Similarly, the other three peaks at 870.0, 873.3 and 880.5 eV correspond to Ni^{+1}, Ni^{+2} and one satellite peak of Ni2p$_{1/2}$.[41,42] The XPS spectrum of S2p (Fig. 1c) shows two peaks at 162.4 and 163.6 eV attributed to S2p$_{3/2}$ and S2p$_{1/2}$.[43] The XPS wide scan survey spectrum of Ni$_3$S$_2$–Ni$_3$N is given in ESI,† S2.1 Fig. S2. The N1s spectrum (Fig. 1d) shows one peak at 398.6 eV corresponding to metal nitrogen bonding.[26] For comparison we also performed the XPS analysis of individual Ni$_3$S$_2$ and Ni$_3$N phases and the information is given in ESI,† S2.2 and 2.3 Fig. S3 and S4. We observed a positive shift of 0.2 eV in the binding energy when comparing the data of Ni2p present in Ni$_3$S$_2$–Ni$_3$N with respect to individual Ni$_3$N. Similarly, a negative shift of 0.3 eV has been observed in the high resolution Ni2p XPS spectra of Ni$_3$S$_2$–Ni$_3$N and individual Ni$_3$S$_2$. The information is given in the ESI,† S2.4 Fig. S5. These results show that there is a charge transfer from Ni$_3$N to Ni$_3$S$_2$ through the interface, which enhances the adsorption of intermediates (H*) on the surface of Ni$_3$S$_2$ by the increased availability of electrons.

The morphological investigation of the catalyst was performed using the field emission scanning electron microscopy (FESEM) technique. Fig. 2a depicts the FESEM image of bare NF. Fig. 2b depicts that of Ni$_3$S$_2$–Ni$_3$N coated on nickel foam. The FESEM images of Ni$_3$S$_2$–Ni$_3$N are given in Fig. 2(c and d). The FESEM images show the sheet-like morphology of the catalyst. To confirm the uniform distribution of all the elements over the catalyst surface, we did EDX elemental mapping of the catalyst. Fig. 2(e–h) show the elemental mapping of Ni$_3$S$_2$–Ni$_3$N where all the elements (Ni, S and N) distributed evenly over the catalyst surface. The nanoscopic features of Ni$_3$S$_2$–Ni$_3$N were examined by high-resolution TEM imaging. The images show a sheet-like structure of Ni$_3$S$_2$–Ni$_3$N (Fig. 3a and b). The presence of both the phases was confirmed by the HR-TEM images (Fig. 3c and d). The interface formation between Ni$_3$S$_2$ and Ni$_3$N was observed with the fringe width of 0.29 nm corresponding to the (110) crystal plane of Ni$_3$S$_2$ and fringe width of
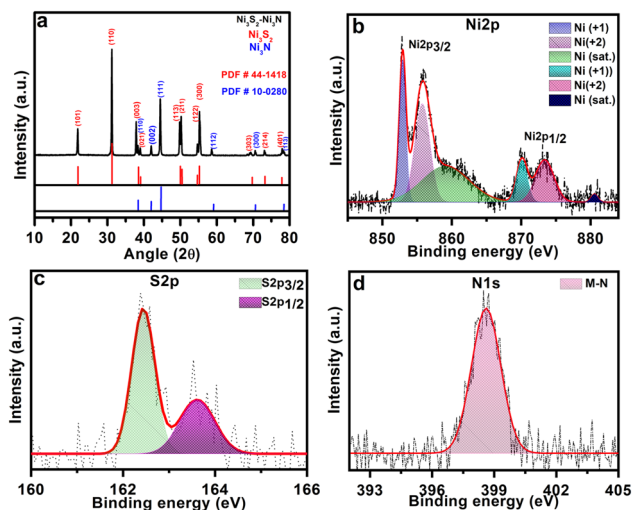

Fig. 1 (a) The PXRD pattern of Ni$_3$S$_2$–Ni$_3$N and (b) the high resolution XPS spectra of Ni 2p, (c) S 2p and (d) N 1s present in Ni$_3$S$_2$–Ni$_3$N.

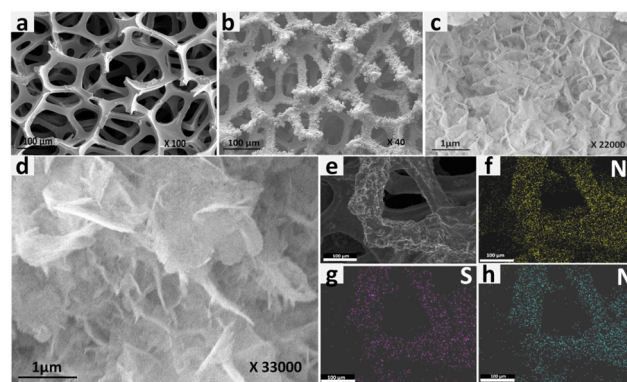**Fig. 2** The SEM images of (a) bare nickel foam and (b) Ni$_3$S$_2$–Ni$_3$N heterostructure nanosheets over NF; (c and d) the sheet-like morphology of Ni$_3$S$_2$–Ni$_3$N and (e–h) elemental mapping of Ni$_3$S$_2$–Ni$_3$N showing the presence of all the elements uniformly over the catalyst surface.
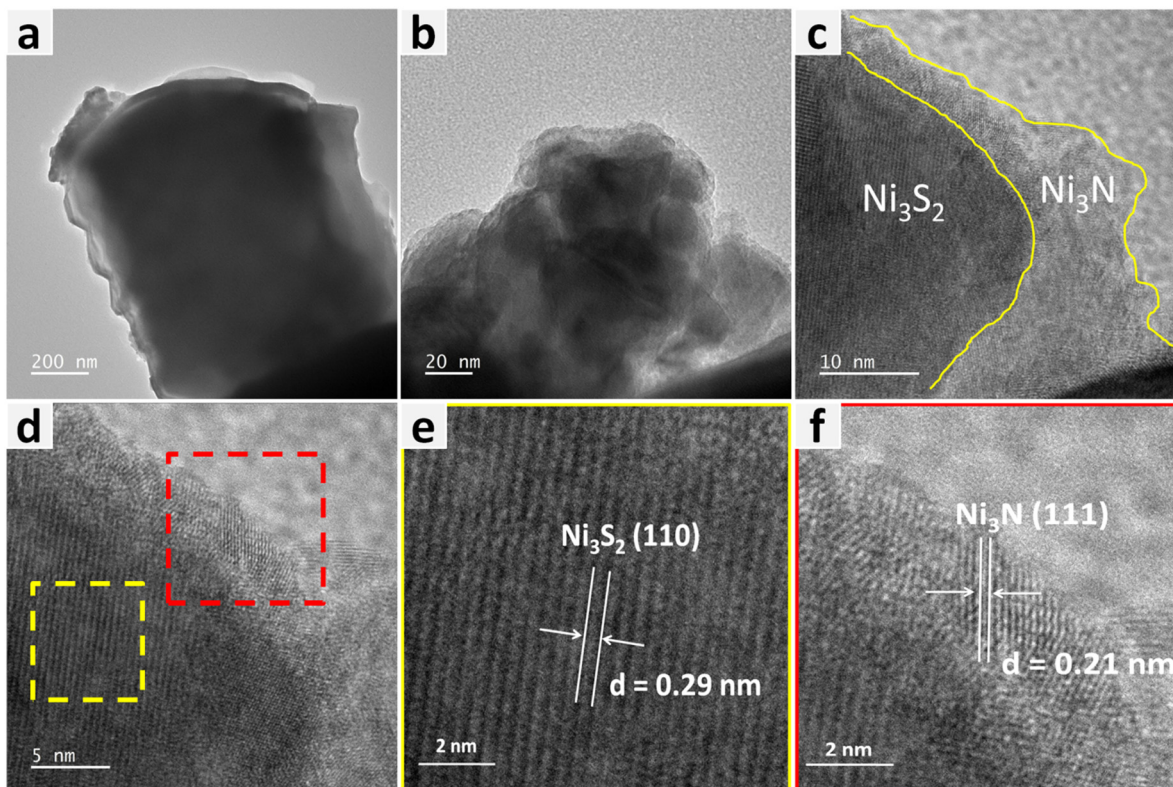
Fig. 3   (a and b) The TEM images of 2-D nanosheets showing the heterostructure of Ni_3S_2–Ni_3N. (c and d) The HRTEM images of Ni_3S_2–Ni_3N showing the formation of an interface between Ni_3S_2 and Ni_3N. (e and f) The HRTEM images showing the presence of Ni_3S_2 and Ni_3N phases with the corresponding fringe widths.

0.21 nm corresponding to the (111) crystal plane of Ni_3N (Fig. 3e and f).[44,45] The superhydrophilic surfaces enable heterogeneous catalysis because they tend to acquire low adsorption energies on their surfaces.[46] The surface behaviour of Ni_3S_2–Ni_3N is equally relevant in heterogeneous catalysis. The contact angle measurement analysis shows that the Ni_3S_2–Ni_3N surface is superhydrophilic as it quickly absorbs a water droplet as soon as it is dribbled on it (Fig. 4a and b), resulting in a contact angle

of $0°$. The surface of the bare nickel foam (NF) was found to be superhydrophobic with a contact angle of $116.7°$ with a water droplet (Fig. 4c and d).

Electrochemical

The hydrogen evolution reactions of Ni_3S_2–Ni_3N, Ni_3S_2 and Ni_3N were performed in an alkaline medium of 1 M KOH (pH = 14). The electrocatalytic properties of Pt/C (coated on a nickel foam) were investigated for comparison under the identical experimental conditions. The polarization curves for the HER are given in Fig. 5a. The overpotential values of 44, 96, 179 and 264 mV are acquired at 10 mA cm^{-2} of current density for Pt/C, Ni_3S_2–Ni_3N, Ni_3N and Ni_3S_2, respectively (Fig. 5b). A table containing the HER activities of recently reported Ni_3N and Ni_3S_2 catalysts is given in ESI,† S3.1 Table S1. Additionally, this table compares the HER activities of recently published reports, which are relevant to our catalyst. To acquire more information about the reaction kinetics, we determined Tafel slope values by plotting the Tafel equation (Fig. 5c). Under alkaline conditions, the HER proceeds along the Volmer–Tafel and Volmer–Heyrovsky routes, which are depicted below:
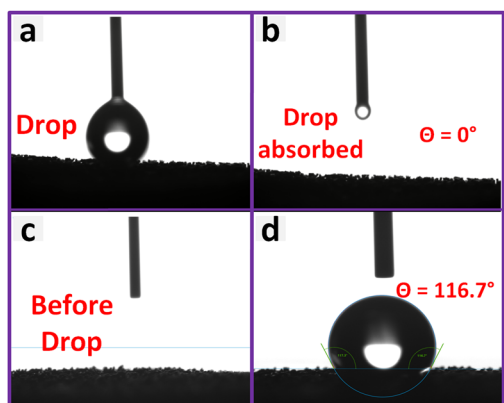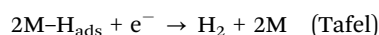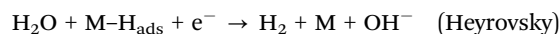
$$H_2O + M + e^- \rightarrow M - H_{ads} + OH^- \quad \text{(Volmer)}$$

$$H_2O + M\text{–}H_{ads} + e^- \rightarrow H_2 + M + OH^- \quad \text{(Heyrovsky)}$$

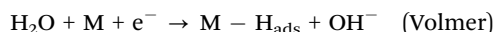$$2M\text{–}H_{ads} + e^- \rightarrow H_2 + 2M \quad \text{(Tafel)}$$

Fig. 4   (a and b) The contact angle measurement of Ni_3S_2–Ni_3N showing superhydrophilic behavior with a contact angle of $0°$. (c and d) Bare nickel foam (NF) showing hydrophobic behavior with a contact angle of $116.7°$.
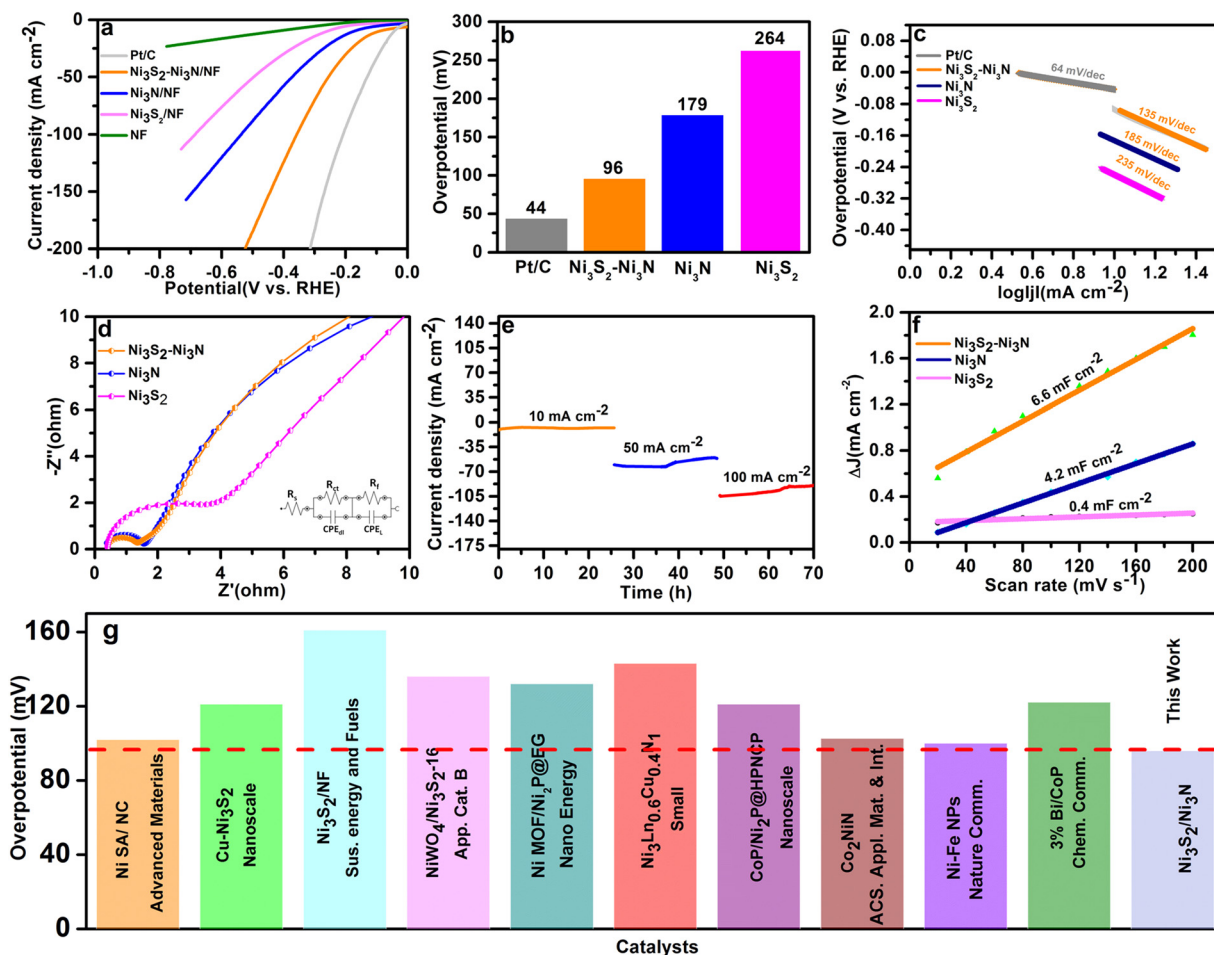
Fig. 5 (a) The polarization curves of all the catalyst for the HER. (b) Overpotential values of the catalysts at 10 mA cm^{-2} of current density. (c) The Tafel plots showing the Tafel slope values of all the catalysts. (d) The Nyquist plots for the determination of R_{ct} using an equivalent circuit shown in the inset image. (e) Stability study using chronoamperometry. (f) Double layer capacitance values of Ni$_3$S$_2$–Ni$_3$N, Ni$_3$S$_2$ and Ni$_3$N. (g) Comparison of our catalyst with the recently reported catalysts for the HER.

The adsorption of the hydrogen on the catalyst's surface is the initial step in both processes. The onset potential of the HER can be evaluated by a Volmer step. With the support of the information based on the aforementioned data, it would be reasonable to assume that the water dissociation during the Volmer stage is significantly boosted, particularly in the case of Ni$_3$S$_2$–Ni$_3$N. Depending upon the value of Tafel slope we can explain the reaction pathway in the Volmer, Tafel, or Heyrovsky steps. The theoretical values of 30, 40 and 120 mV dec^{-1} are obtained when Tafel, Heyrovsky and Volmer are the rate determining steps. Our findings for Ni$_3$S$_2$–Ni$_3$N revealed that the reaction follows a Volmer–Heyrovsky pathway with a Tafel slope value of 135 mV dec^{-1}. The Tafel slope values for Ni$_3$N and Ni$_3$S$_2$ are 185 and 235 mV dec^{-1}. The concerned catalyst shows favourable HER kinetics by depicting a lower Tafel slope value than those of the individual phases. The strong interfacial contacts seem to enable a quicker electron transit over the interface, as shown by the charge transfer resistance, assessed using electrochemical impedance spectroscopy. Fig. 5d shows the Nyquist plots at an applied potential of 100 mV. By fitting the equivalent circuit shown in Fig. 5d, all the relevant

parameters are determined. The charge-transfer resistance (R_{ct}) is lower for Ni$_3$S$_2$–Ni$_3$N with respect to the other catalysts. The lower value of R_{ct} reflects both a decent rate of charge-transfer between the electrode surface and the electrolyte and a greater amount of electrochemically active sites on the electrode surface. These Nyquist plots also indicate an excellent HER activity of Ni$_3$S$_2$–Ni$_3$N. The table showing the values of R_s and R_{ct} is provided in ESI,† S3.2 Table S2. The stability of the Ni$_3$S$_2$–Ni$_3$N catalyst was determined using chronoamperometry, continuously running for 70 h (Fig. 5e). Even after 70 hours of stability study, no significant change in the current density was noticed. The XPS analysis and PXRD study of the catalyst after the stability test have been done and the data are provided in ESI,† S3.3, S3.4 and Fig. S6, S7. The XPS and PXRD details confirm that the structure of the catalyst remains intact even after the stability experiment. Both the phases (Ni$_3$S$_2$ and Ni$_3$N) with the corresponding planes were present in the PXRD pattern. Electrochemically active surface areas (ECSAs) were calculated using the double-layer capacitance (C_{dl}) values retrieved from cyclic voltammetry curves in the non-faradaic region (Fig. 5f). The calculated ECSA values for Ni$_3$S$_2$–Ni$_3$N,

Ni_3N and Ni_3S_2 are 16.5, 10.5 and 1 cm^{-2}, respectively. The higher value of ECSA indicates that there are abundant active sites on the catalyst surface. Cyclic voltammetry curves used for the calculation of the ECSA values are given in ESI,† S3.5 Fig. S8. A comparison of the overpotential of Ni_3S_2–Ni_3N with those of recently reported catalysts is given in Fig. 5g.

Conclusions

Herein, an appropriate nanostructuring and judicious selection of the catalyst composition lead to the formation of an excellent electrocatalyst. Plentiful Ni_3S_2–Ni_3N interface that is formed *in-situ* in-between the layers of Ni_3N and Ni_3S_2 creates a heterostructure with highly improved HER parameters. The procedure inherits the benefits of the abundant interfaces formed in addition to the individual components in the catalyst. The catalyst is superhydrophilic in nature as shown by the contact angle measurement, enhances the ionic transfer from the electrolyte to the electrode surface and facilitates the mass transport mechanism. XPS studies have revealed charge transfer from Ni_3N to Ni_3S_2, which provided abundant electrons on the surface of Ni_3S_2 for better interaction with the H^+ ion. The Ni_3S_2–Ni_3N catalyst displayed excellent HER activity in an alkaline medium with an overpotential of 96 mV to drive a current density of 10 mA cm^{-2}. Chronoamperometric study exhibits no significant variation in the current density even after 70 hrs of stability experiment in an alkaline medium. It should be noted that the current densities used for the stability experiment are quite a bit higher than usual. The above study furnishes an important clue towards the possible manipulation of the composition of metal sulphide and nitride at the nanoscale to create a desirable heterostructure for efficient electrochemical applications.

Author contributions

V. P., A. G. and V. B. conceived the project. A. G. and V. P. designed and performed the experiments. A. G. and V. B. wrote and revised the paper. All the authors discussed the results and commented on the manuscript.

Conflicts of interest

There are no conflicts to declare.

Acknowledgements

Notes and references

1 M. Ji and J. Wang, *Int. J. Hydrogen Energy*, 2021, **46**, 38612–38635.

2 S. Sharma and S. K. Ghoshal, *Renewable Sustainable Energy Rev.*, 2015, **43**, 1151–1158.

3 J. Hou, Y. Wu, B. Zhang, S. Cao, Z. Li and L. Sun, *Adv. Funct. Mater.*, 2019, **29**, 1808367.

4 J. Wang, Z. Wei, S. Mao, H. Li and Y. Wang, *Energy Environ. Sci.*, 2018, **11**, 800–806.

5 X. Li, C. Wang, S. Zheng, H. Xue, Q. Xu, P. Braunstein and H. Pang, *J. Colloid Interface Sci.*, 2022, **624**, 443–449.

6 V. K. Abdelkader-Fernández, D. M. Fernandes, L. Cunha-Silva, A. J. S. Fernandes and C. Freire, *Electrochim. Acta*, 2021, **389**, 138719.

7 Z. Manappadan and K. Selvaraj, *Energy Adv.*, 2022, **1**, 886–899.

8 C. Meng, Z. Wang, L. Zhang, X. Ji, X. Chen and R. Yu, *Inorg. Chem.*, 2022, **61**, 9832–9839.

9 R. Kumar, A. Gaur, T. Maruyama, C. Bera and V. Bagchi, *ACS Appl. Mater. Interfaces*, 2020, **12**, 57898–57906.

10 J. Zhou, C. Huang, Q. Zhou, Y. Xie, L. Yang, L. Yu and Y. Yu, *Inorg. Chem.*, 2022, **61**, 9318–9327.

11 Y. Lu, X. Zheng, Y. Liu, J. Zhu, D. Li and D. Jiang, *Inorg. Chem.*, 2022, **61**, 8328–8338.

12 S. M. El-Refaei, P. A. Russo and N. Pinna, *ACS Appl. Mater. Interfaces*, 2021, **13**, 22077–22097.

13 W. He, H. Liu, J. Cheng, J. Mao, C. Chen, Q. Hao, J. Zhao, C. Liu, Y. Li and L. Liang, *Nanoscale*, 2021, **13**, 10127–10132.

14 K. L. Zhou, C. B. Han, Z. Wang, X. Ke, C. Wang, Y. Jin, Q. Zhang, J. Liu, H. Wang and H. Yan, *Adv. Sci.*, 2021, **8**, 2100347.

15 J. Wu, Q. Zhang, K. Shen, R. Zhao, W. Zhong, C. Yang, H. Xiang, X. Li and N. Yang, *Adv. Funct. Mater.*, 2022, **32**, 2107802.

16 H.-F. Wang, L. Chen, H. Pang, S. Kaskel and Q. Xu, *Chem. Soc. Rev.*, 2020, **49**, 1414–1448.

17 S. Xu, Q. Huang, J. Xue, Y. Yang, L. Mao, S. Huang and J. Qian, *Inorg. Chem.*, 2022, **61**, 8909–8919.

18 K. L. Zhou, Z. Wang, C. B. Han, X. Ke, C. Wang, Y. Jin, Q. Zhang, J. Liu, H. Wang and H. Yan, *Nat. Commun.*, 2021, **12**, 3783.

19 Z. Liu, D. Jiang, L. Yang, J. Yu, X. Li, X. Liu, L. Zhao, X. Zhang, F. Han, W. Zhou and H. Liu, *Nano Energy*, 2021, **88**, 106302.

20 R. A. Mir, S. Upadhyay, R. A. Rather, S. J. Thorpe and O. P. Pandey, *Energy Adv.*, 2022, **1**, 438–448.

21 A. Badreldin, A. Nabeeh, Z. K. Ghouri, J. Abed, N. Wang, Y. Wubulikasimu, K. Youssef, D. Kumar, M. K. Stodolny, K. Elsaid, E. H. Sargent and A. Abdel-Wahab, *ACS Appl. Mater. Interfaces*, 2021, **13**, 53702–53716.

22 X. Peng, C. Pi, X. Zhang, S. Li, K. Huo and P. K. Chu, *Sustainable Energy Fuels*, 2019, **3**, 366–381.

23 H. Jin, X. Wang, C. Tang, A. Vasileff, L. Li, A. Slattery and S.-Z. Qiao, *Adv. Mater.*, 2021, **33**, 2007508.

24 Z. Liu, M. Zha, Q. Wang, G. Hu and L. Feng, *Chem. Commun.*, 2020, **56**, 2352–2355.

25 T. Kou, M. Chen, F. Wu, T. J. Smart, S. Wang, Y. Wu, Y. Zhang, S. Li, S. Lall, Z. Zhang, Y.-S. Liu, J. Guo, G. Wang, Y. Ping and Y. Li, *Nat. Commun.*, 2020, **11**, 590.

26 D. Gao, J. Zhang, T. Wang, W. Xiao, K. Tao, D. Xue and J. Ding, *J. Mater. Chem. A*, 2016, **4**, 17363–17369.

27 B. Liu, B. He, H.-Q. Peng, Y. Zhao, J. Cheng, J. Xia, J. Shen, T.-W. Ng, X. Meng, C.-S. Lee and W. Zhang, *Adv. Sci.*, 2018, **5**, 1800406.

28 M. Gao, L. Chen, Z. Zhang, X. Sun and S. Zhang, *J. Mater. Chem. A*, 2018, **6**, 833–836.

29 M. Wang, W. Ma, Z. Lv, D. Liu, K. Jian and J. Dang, *J. Phys. Chem. Lett.*, 2021, **12**, 1581–1587.

30 H. Zhou, Y. Wang, R. He, F. Yu, J. Sun, F. Wang, Y. Lan, Z. Ren and S. Chen, *Nano Energy*, 2016, **20**, 29–36.

31 P. Jiang, Q. Liu and X. Sun, *Nanoscale*, 2014, **6**, 13440–13445.

32 L.-L. Feng, G. Yu, Y. Wu, G.-D. Li, H. Li, Y. Sun, T. Asefa, W. Chen and X. Zou, *J. Am. Chem. Soc.*, 2015, **137**, 14023–14026.

33 Y. Ding, X. Du and X. Zhang, *ChemCatChem*, 2021, **13**, 1824–1833.

34 S.-Y. Lu, S. Li, M. Jin, J. Gao and Y. Zhang, *Appl. Catal., B*, 2020, **267**, 118675.

35 Z. Wu, Y. Feng, Z. Qin, X. Han, X. Zheng, Y. Deng and W. Hu, *Small*, 2022, 2106904n/a.

36 X. Tong, Y. Li, Q. Ruan, N. Pang, Y. Zhou, D. Wu, D. Xiong, S. Xu, L. Wang and P. K. Chu, *Adv. Sci.*, 2022, **9**, 2104774.

37 H. Su, S. Song, S. Li, Y. Gao, L. Ge, W. Song, T. Ma and J. Liu, *Appl. Catal., B*, 2021, **293**, 120225.

38 J. Liu, Y. Wang, Y. Liao, C. Wu, Y. Yan, H. Xie and Y. Chen, *ACS Appl. Mater. Interfaces*, 2021, **13**, 26948–26959.

39 L. Zhang, X. Gao, Y. Zhu, A. Liu, H. Dong, D. Wu, Z. Han, W. Wang, Y. Fang, J. Zhang, Z. Kou, B. Qian and T.-T. Wang, *Nanoscale*, 2021, **13**, 2456–2464.

40 G. S. Shanker and S. Ogale, *ACS Appl. Energy Mater.*, 2021, **4**, 2165–2173.

41 T. Wu, E. Song, S. Zhang, M. Luo, C. Zhao, W. Zhao, J. Liu and F. Huang, *Adv. Mater.*, 2022, **34**, 2108505.

42 M. Wang, L. Zhang, J. Pan, M. Huang and H. Zhu, *Nano Res.*, 2021, **14**, 4740–4747.

43 Q. Liu, L. Xie, Z. Liu, G. Du, A. M. Asiri and X. Sun, *Chem. Commun.*, 2017, **53**, 12446–12449.

44 W. Zhou, X. Cao, Z. Zeng, W. Shi, Y. Zhu, Q. Yan, H. Liu, J. Wang and H. Zhang, *Energy Environ. Sci.*, 2013, **6**, 2216–2221.

45 M.-S. Balogun, Y. Zeng, W. Qiu, Y. Luo, A. Onasanya, T. K. Olaniyi and Y. Tong, *J. Mater. Chem. A*, 2016, **4**, 9844–9849.

46 X. Shan, J. Liu, H. Mu, Y. Xiao, B. Mei, W. Liu, G. Lin, Z. Jiang, L. Wen and L. Jiang, *Angew. Chem., Int. Ed.*, 2020, **59**, 1659–1665.